


Article

Early Cretaceous A-Type Acidic Magmatic Belt in Northern Lhasa Block: Implications for the Evolution of the Bangong–Nujiang Ocean Lithosphere

Deng Xiao , Xinjie Yang *, Chao Teng, Tianshe Cheng, Ning Zhu and Jun Cao

Cores and Samples Center of Natural Resources, China Geological Survey, Langfang 065201, China; xiaodeng@mail.cgs.gov.cn (D.X.); tc.1985@163.com (C.T.); chengtianshe515@163.com (T.C.); ningzhu@cug.edu.cn (N.Z.); cjun@mail.cgs.gov.cn (J.C.)

* Correspondence: yxinjie@mail.cgs.gov.cn; Tel.: +86-180-0110-3396

Abstract: A-type granites have been the subject of considerable interest due to their distinct anorogenic geological background. The A-type and arc-related granites are crucial in deciphering the evolution of the ocean closure and continental collision in the Tibet Plateau. The demise of the Bangong–Nujiang suture zone (BNSZ) and the Yarlung–Tsangpo suture zone was accompanied by the emplacement of volumes of syn-collisional and post-collisional granites. Controversy has persisted regarding the contribution of the collisional granites within the Lhasa Block to the growth of the Tibetan Plateau. This study provides key evidence about the evolution of the Lhasa Block and Bangong–Nujiang Ocean (BNO) by the newly documented 1200 km long, Early Cretaceous A-type acidic magmatic belt. The resolution was achieved through the utilization of petrology, whole-rock geochemistry, zircon U–Pb geochronology, and in situ zircon Hf isotope analysis of the Burshulaling Granites in the eastern segment and previous existing data in the central and western segment of the Lhasa Block. The Burshulaling Granites are characterized as peraluminous, high-K calc-alkaline series, indicating a post-collision setting with high temperature and low pressure. The zircon grains from two granite samples yield $^{206}\text{Pb}/^{238}\text{U}$ ages of 115–113 Ma. In situ zircon Hf analyses with $^{206}\text{Pb}/^{238}\text{U}$ ages give $\varepsilon_{\text{Hf}}(t)$ of -6.2 – -0.6 , showing prominent characteristics of crust–mantle interaction. Granites from east to west exhibit whole-rock geochemical and geochronological similarities that fall within the well-constrained Early Cretaceous time frame (117–103 Ma) and track post-collisional A-type acidic magmatic belt along BNSZ. We argue that this magmatism resulted from slab break-off or orogenic root detachment, leading to melting and mixing of the lower crust. Meanwhile, this study indicates the existence of the Bangong–Nujiang Ocean southward subduction or a collapse following an Andean-type orogen.

Keywords: Bangong–Nujiang Ocean; Early Cretaceous Burshulaling Granites; A-type acidic magmatic belt; subduction polarity; orogenic collapse



Citation: Xiao, D.; Yang, X.; Teng, C.; Cheng, T.; Zhu, N.; Cao, J. Early Cretaceous A-Type Acidic Magmatic Belt in Northern Lhasa Block: Implications for the Evolution of the Bangong–Nujiang Ocean Lithosphere. *Minerals* **2024**, *14*, 681. <https://doi.org/10.3390/min14070681>

Academic Editors: Rubén Díez-Fernández, Shuang-Qing Li and Long Chen

Received: 25 May 2024
Revised: 20 June 2024
Accepted: 28 June 2024
Published: 29 June 2024



Copyright: © 2024 by the authors. Licensee MDPI, Basel, Switzerland. This article is an open access article distributed under the terms and conditions of the Creative Commons Attribution (CC BY) license (<https://creativecommons.org/licenses/by/4.0/>).

1. Introduction

A-type granites are generally recognized by high concentrations of SiO_2 , FeO^{T} , $\text{Na}_2\text{O} + \text{K}_2\text{O}$, Rare Earth Elements (REE), and Ga/Al ratios, but low in Eu (<0.30) [1,2], Al_2O_3 , Sr, Ba, and Ti [3–6]. A-type granites are different from S-type and I-type granites due to their geochemical compositions being more influenced by the formation environment, featuring relatively high temperature–low pressure rather than their parent rocks [1,7,8]. These unique geochemical properties limit the formation of A-type granites only in intra-plate and post-collision settings [9,10].

The Bangong–Nujiang suture zone (BNSZ) is in the central Tibetan Plateau, between the Lhasa Block and the Qiangtang Block, which marks the closure trace of the Bangong–Nujiang Ocean (BNO) and represents a major Tethyan suture zone in Tibet

(Figure 1a) [11–16]. In addition to the previously documented Cenozoic Indo-Asian collision, there is growing evidence that the late Mesozoic Lhasa–Qiangtang collision may have contributed to the elevation of the Tibetan Plateau [15,16]. In recent decades, the discovery of world-class metallogenic belts within the BNSZ has attracted the attention of the international community [17]. Several studies suggested that BNSZ opened during the Permian–Jurassic and closed in the Early Jurassic–Late Cretaceous due to northward subduction [18–20]. However, based on the structural styles and rock assemblage of BNSZ consisting of (ophiolitic) mélangé, arc-related magmatic rocks, and flysch-type sediments, other researchers argue that there is an existence of southward subduction [13,21]. During oceanic closure, the detachment of the oceanic and continental lithosphere due to differences in buoyancy has resulted in the slab break-off accompanied by partial melting of different source regions [22]. Continental collisions are accompanied by syn-collisional and post-collisional magmatism, which is attributed to the partial melting of varying source regions [14,23,24]. However, the northward subduction of the Yarlung–Tsangpo Ocean was also accompanied by the formation of arc-related magmatism. This has led to controversy regarding which subduction was responsible for its genesis [25]. Consequently, the presence of regional outcrops of syn-collisional and post-collisional granites with petrologic, geochemical, and geochronologic correlations is a significant indicator that can be utilized to reveal the process of oceanic closure.

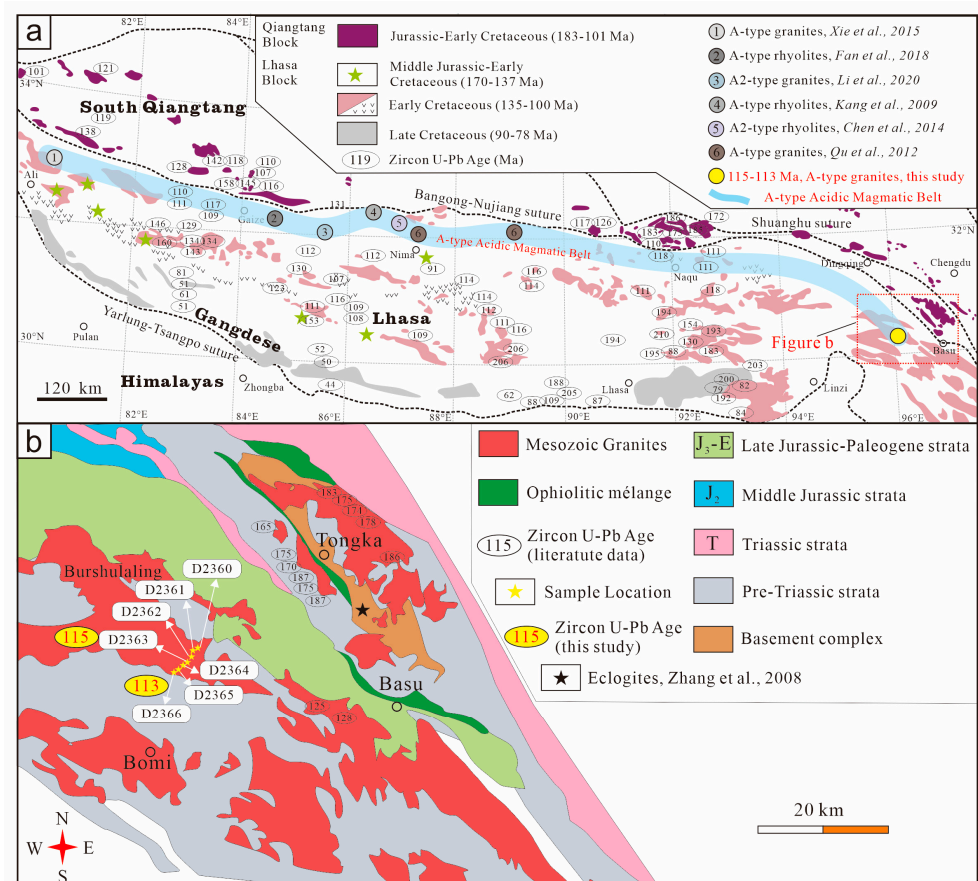


Figure 1. (a) Tectonic subdivision of the Tibetan Plateau [11,15]. Age data are from Zhu et al. (2012), Zhang et al. (2012), and Peng et al. (2020) [11,15,26–32]. (b) Geological map of the study area [26,33].

This study provides a combined petrological, geochemical, zircon U–Pb dating, and in situ Hf isotopic study of the Burshulaling Granites in the eastern segment and compared with pre-existing data in the central and western segment of the BNSZ. The geochemical characteristics indicate that the Burshulaling Granites are peraluminous, high-K calc-

alkaline, and formed in a high temperature–low pressure environment at ca. 115–113 Ma. Noteworthy is the presence of a 1200 km long, A-type acidic magmatic belt within the well-constrained time range of Early Cretaceous along BNSZ. This A-type acidic magmatic belt was formed after the collision between the Lhasa and Qiangtang Blocks or orogenic collapse following an Andean-type orogen in southern Tibet. The belt and the previously widely reported arc-related granites collectively illustrate the demise process of the BNO by southward subduction of the lithosphere or the transition of the Lhasa Block from a compressional deformation to an extensional deformation.

2. Geological Background

The Tibetan Plateau, situated within the eastern Tethys tectonic domain, is segmented into the Bayan Har–Garze Block, the North Qiangtang Block, the South Qiangtang Block, and the Lhasa Block from north to south (Figure 1a). The BNSZ documents the remnants of the collision of Lhasa and Qiangtang Blocks. This geological feature is well-established and can be traced from Bangong Lake through the areas of Changze, Dongqiao, Nagchu, Dingqing, and Basu and southeastward along the Nujiang River (Figure 1a) [15,16,34]. In contrast to some orogenic belts with well-defined boundaries, BNSZ is primarily composed only of some irregularly distributed ophiolites (e.g., Dingqing ophiolite, Amdo ophiolite, Beila ophiolite, Pungco ophiolite) and siliciclastic mélanges (e.g., Mugangan-gri Complex) [15,16,35–40]. Within the suture zone and on both sides, fragments of the Bangong–Nujiang oceanic plateaus erupted at peaking ages of ca. 185 Ma and ca. 121 Ma, which are widely preserved [16,41,42]. Eclogites have been reported in the Basu area adjacent to the study area and are interpreted as a record of subduction subsequent exhumation within the eastern BNSZ during the Jurassic (Figure 1b) [33].

Despite extensive research conducted on the BNSZ over the years, there is controversy regarding its opening period, subduction direction, and closure timing. Radiolarian in siliceous rocks suggests the BNO opened in the Middle Jurassic–Early Cretaceous [43]. Re-Os isotopes of peridotites in the Bangong Lake and Dongqiao areas suggest that ophiolites were formed in the Late Permian [44]. The Early Permian basic dykes in the Naqu area have also been interpreted as evidence of the opening of the BNO [45]. The Late Jurassic or Early Cretaceous of the BNO closure are also disputed, and the controversy focuses on which the angular unconformity of the overlying sedimentary rocks represents the final oceanic closure [46,47]. There have been two main views on the subduction direction of the BNO, including (i) solely northward subduction, mainly based on the Jurassic–Cretaceous calc-alkaline arc-related magmatism developed along the southern edge of Qiangtang Block and subduction-related sedimentary stratigraphy [19,25]; (ii) the existence of southward subduction, based on the Jurassic and Early Cretaceous arc-related calc-alkaline series magmatic rocks in the northern edge of Lhasa Block [13,14,21,27–32]. However, the origin of the magmatic rocks within the Lhasa Block is controversial. Whether these magmatic rocks are the product of the northward subduction of the Yarlung–Tsangpo Ocean or the southward subduction of the BNO is still disputed [25].

There are large-scale Mesozoic–Cenozoic igneous rocks distributed within the Lhasa Block, about 2500 km long and 150–300 km wide from north to south [12]. The Lhasa Block exhibits distinct characteristics in the north and south. Juvenile magmatic rocks, including the Mesozoic–Early Cenozoic Gangdese batholiths and the Lingzizong volcanic succession, dominate the south Lhasa Block. In contrast, the north mainly comprises widely distributed Mesozoic and minor Paleozoic sedimentary rocks [15,48,49]. In contrast to the 300 km wide Central and Western Lhasa Blocks, the Eastern Lhasa Block went through the Cenozoic Indo–Eurasia collision, resulting in a width of less than 150 km [12,50,51]. The Burshulaling Granites are situated in the northeast of Bomi County, Tibet, and geospatially, it is now close to both the BNSZ and the Gangdese batholith (Figure 1b). The Burshulaling Granites are regionally exposed to more than 300 km². It is dominated by monzogranite and granodiorite, followed by a small amount of quartz-diorite and porphyritic quartz-diorite. There are also various views on the formation age of Jurassic to Early Cretaceous

by the K-Ar dating [50]. Although the magmatism of the Burshulaling area has been poorly studied, it is generally recognized in regional geologic surveys as a component of the Northern Lhasa Block [50]. The magmatic composition during the Early Cretaceous of the Northern Lhasa Block is predominantly high-K calc-alkaline. Still, the presence of medium-low-K granites can be observed in some areas. The zircon $\varepsilon_{\text{Hf}}(t)$ values exhibit a general increasing trend from the eastern segment (-10.0 to $+0.9$) to the central segment (-1.5 to $+10.1$) and then to the western segment ($+4.7$ to $+18.4$) [21]. There are no inherited zircon ages older than Early Cretaceous reported in the Northern Lhasa Block.

3. Sample Description and Petrography

The Burshulaling Granites lie between the Gangdese batholith and the BNSZ and intrude into the Carboniferous Nuocuo Formation (C_1n) and Laigu Formation (C_2P_1l) in the study area. Nuocuo Formation and Laigu Formation are widely distributed in eastern Tibet, and both are composed of conglomerate-bearing slates, sandstone, and bioclastic limestone. The Burshulaling Granites mainly consist of (biotite) granite-monzogranite, quartz-diorite, and quartz monzonite. For geochemical analyses, five biotite monzogranite samples (D2360, D2362, D2363, D2364, D2365) and two quartz monzonite samples (D2361, D2366) were selected. For U-Pb dating and in situ Hf isotope analysis, samples D2363 and D2366 were selected. All samples were collected at nearly equal intervals from edge to center, with samples taken from the tunnels (D2360, D2361, D2362, D2363, D2366) in covered areas. Biotite monzogranite is gray-white, and its main minerals are plagioclase, K-feldspar, quartz, and biotite. The accessory minerals are mainly zircon and apatite (Figure 2a,b,d,e). The plagioclase grains from biotite monzogranite exhibit a well-developed zoning structure (Figure 2d). Quartz monzonite is gray-white and mainly comprises plagioclase, K-feldspar, quartz, and biotite, with accessory zircon, epidote, sphene, and apatite (Figure 2c,f). The proportion of feldspar in granite is relatively constant (ca. 70 vol.%), but quartz monzonite has a higher concentration of K-feldspar (>50 vol.%). The content of quartz exhibits variability, ranging from >25 vol.% (biotite monzogranite, Figure 2d,e) to ca. 10 vol.% (quartz monzonite, Figure 2f). No phase transition features were observed in the Burshulaling Granites.

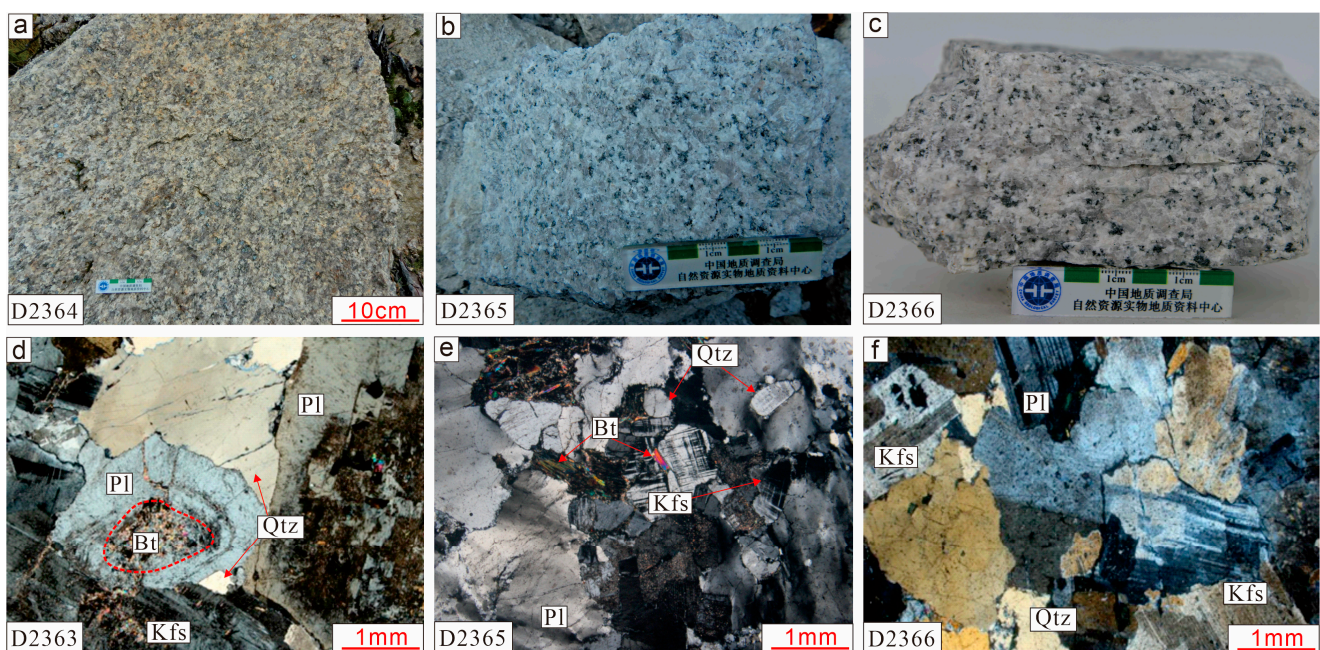


Figure 2. (a–c) Macroscopic texture and (d–f) Photomicrographs of the Burshulaling Granites (cross-polarized light). Abbreviations: Qtz = quartz, Kfs = K-feldspar, Pl = plagioclase, Bt = biotite.

4. Analytical Methods and Results

Zircon separation, Cathodoluminescence (CL) photomicrographs, and major and trace elements analysis were carried out at the Regional Geological Survey of Hebei Province, Langfang, China. Major and trace elements, including REE compositions, were analyzed by inductively coupled plasma–optical emission spectroscopy (ICP–OES; Leeman Prodigy) with high–dispersion Echelle optics. Loss on ignition (LOI) values was determined by heating 1 g of sample in a furnace at 950 °C for several hours before being cooled in a desiccator and reweighed. Analytical uncertainties are generally better than 1% for major elements and better than 2% for trace elements.

Zircon U–Pb dating, in situ Hf isotope ratio, and trace-element analysis were conducted at Wuhan Sample Solution Analytical Technology Co., Ltd., Wuhan, China. Details on the operating conditions and data processing procedures are identical to Liu et al. (2010) and Hu et al. (2015) [52,53]. The zircon U–Pb dating and trace element analysis of zircon were simultaneously conducted by LA–ICP–MS. Zircon 91500 and glass NIST610 were used as external standards for U–Pb dating and trace-element calibration, respectively. Experiments of in situ Hf isotope ratio analysis were conducted on the same spots or the same age domains using a Neptune Plus MC–ICP–MS (Thermo Fisher Scientific, Germany) in combination with a Geolas HD excimer ArF laser ablation system (Coherent, Göttingen, Germany) that was hosted. The measured values agreed with the recommended values to within 2σ .

4.1. Zircon U–Pb Geochronology Results

Zircons from one biotite monzogranite (D2363) and one quartz monzonite (D2366) are used for U–Pb geochronology analysis. The representative zircon CL images and the dating positions are given in Figure 3a,c with red or yellow circles. Details of zircon U–Pb analyses, including isotopic contents, ratios, errors, and ages, are summarized in Table 1. Zircon grains are mostly euhedral with lengths of 100–300 μm and widths of 50–150 μm . For sample D2363, the analyses of the 22 zircons from sample yield $^{206}\text{Pb}/^{238}\text{U}$ ages ranging from 112 ± 1.3 Ma to 120 ± 2.1 Ma, with a weighted mean age of 114.9 ± 0.9 Ma (mean squared weighted deviation, MSWD = 2.7; Figure 3b). Additionally, an inherited zircon core was identified in the biotite monzogranite (D2363–25) with an irregular zoned structure (Figure 3a, position 25). The inherited zircon from sample D2363 yielded a $^{206}\text{Pb}/^{238}\text{U}$ age of 928 ± 18 Ma (Figure 3b). The analysis of 22 zircons from sample D2366 yielded $^{206}\text{Pb}/^{238}\text{U}$ ages ranging from 112 ± 1.1 Ma to 115 ± 2.1 Ma, with a weighted mean age of 113.1 ± 0.6 Ma (MSWD = 0.57; Figure 3d). No metamorphic rims have been found in the two samples. All zircon grains exhibit clear oscillatory zoning (Figure 3a,c). The analyzed zircon from biotite monzogranite with high concordance (>95%, 23 zircon grains) have varying Th (740–3702 ppm) and U content (1527–6447 ppm), with Th/U ratios ranging from 0.12 to 1.16 (Table 1). The analyzed zircon from quartz monzonite with high concordance (>95%, 22 zircon grains) have varying Th content (411–1312 ppm) and U content (624–1816 ppm), with high Th/U ratios ranging from 0.37 to 0.62 (Table 1). The CL characteristics and Th/U ratios of the two samples agree with a magmatic origin [54]. The timing of granite crystallization is considered to be between 115 and 113 Ma, based on the core–rim structure, while the age of the protolith is estimated to be 928 Ma.

4.2. In Situ Zircon Hf Isotope Results

A total of 22 zircon grains from biotite monzogranite (D2363) and 22 zircon grains from quartz monzonite (D2366) were carried out for in situ zircon Hf isotopes, except four grains from sample D2363 and two grains from sample D2366 have high $^{176}\text{Yb}/^{177}\text{Hf}$ ration (>15%) which were not adopted. The Hf isotopic results are given in Table 2. Twenty-one analyses with $^{206}\text{Pb}/^{238}\text{U}$ ages of ca. 115 Ma from sample D2363 yielded $\varepsilon_{\text{Hf}}(t)$ values from -6.2 to 0.6 (Figure 4), which corresponded to crustal ages (T_{DM}^{C}) of 1.11–1.56 Ga. Twenty-two analyses with $^{206}\text{Pb}/^{238}\text{U}$ ages of ca. 113 Ma from sample D2366 yielded $\varepsilon_{\text{Hf}}(t)$ values from -3.6 to 0.2 , corresponding to crustal ages (T_{DM}^{C}) of 1.15–1.40 Ga.

Table 1. LA-ICP-MS zircon U-Pb data of the Burshulaling Granites.

Point	Content (ppm)			Th/U	Isotopic Ratios				Isotopic Ages (Ma)	
	Pb	Th	U		$^{207}\text{Pb}/^{235}\text{U}$	1 σ	$^{206}\text{Pb}/^{238}\text{U}$	1 σ	$^{206}\text{Pb}/^{238}\text{U}$	1 σ
D2363-02	47.2	889	2256	0.4	0.1262	0.0032	0.0185	0.0002	118	1.2
D2363-05	14.0	406	654	0.6	0.1140	0.0054	0.0179	0.0002	114	1.3
D2363-06	14.7	513	647	0.8	0.1246	0.0051	0.0179	0.0002	115	1.5
D2363-07	16.1	401	742	0.5	0.1226	0.0061	0.0188	0.0003	120	2.1
D2363-08	11.4	330	531	0.6	0.1143	0.0049	0.0178	0.0002	114	1.4
D2363-09	48.1	1632	2119	0.8	0.1264	0.0035	0.0185	0.0002	118	1.1
D2363-11	135.6	3702	6447	0.6	0.1267	0.0031	0.0183	0.0002	117	1.4
D2363-12	23.2	530	1131	0.5	0.1162	0.0040	0.0177	0.0002	113	1.1
D2363-13	93.6	1418	4579	0.3	0.1193	0.0028	0.0184	0.0002	117	1.0
D2363-14	5.3	159	245	0.6	0.1217	0.0075	0.0182	0.0003	116	1.8
D2363-15	11.1	286	510	0.6	0.1239	0.0065	0.0185	0.0002	118	1.5
D2363-16	9.5	252	445	0.6	0.1158	0.0059	0.0179	0.0003	115	1.7
D2363-17	3.2	100	139	0.7	0.1247	0.0085	0.0182	0.0004	116	2.4
D2363-19	16.4	440	777	0.6	0.1199	0.0059	0.0180	0.0003	115	1.7
D2363-20	11.3	492	477	1.0	0.1242	0.0064	0.0179	0.0002	114	1.6
D2363-21	69.0	1080	3466	0.3	0.1270	0.0033	0.0177	0.0001	113	0.9
D2363-22	74.1	1105	3747	0.3	0.1225	0.0030	0.0178	0.0001	114	0.9
D2363-23	16.7	486	793	0.6	0.1117	0.0045	0.0175	0.0002	112	1.3
D2363-24	19.3	922	791	1.2	0.1248	0.0049	0.0178	0.0002	114	1.3
D2363-25	39.3	143	227	0.6	1.4943	0.0561	0.1550	0.0033	929	18.6
D2363-26	10.4	69	555	0.1	0.1217	0.0048	0.0178	0.0002	114	1.2
D2363-27	8.7	250	401	0.6	0.1255	0.0062	0.0181	0.0002	115	1.6
D2363-30	43.4	811	2144	0.4	0.1232	0.0035	0.0178	0.0002	114	1.0
D2366-01	26.9	686	1280	0.5	0.1196	0.0041	0.0175	0.0002	112	1.1
D2366-02	37.4	772	1816	0.4	0.1176	0.0037	0.0178	0.0002	114	1.1
D2366-04	14.1	780	529	1.5	0.1196	0.0056	0.0176	0.0002	112	1.3
D2366-05	25.1	590	1194	0.5	0.1150	0.0042	0.0176	0.0002	112	1.2
D2366-06	4.0	116	174	0.7	0.1212	0.0087	0.0180	0.0003	115	2.1
D2366-07	12.1	320	556	0.6	0.1244	0.0061	0.0176	0.0002	112	1.5
D2366-09	15.7	424	721	0.6	0.1132	0.0051	0.0177	0.0002	113	1.2
D2366-10	2.7	97	115	0.8	0.1081	0.0100	0.0175	0.0004	112	2.5
D2366-11	29.7	594	1433	0.4	0.1209	0.0042	0.0176	0.0002	112	1.0
D2366-12	26.8	1312	1082	1.2	0.1184	0.0047	0.0178	0.0002	114	1.4
D2366-13	3.4	104	154	0.7	0.1213	0.0113	0.0175	0.0004	112	2.2
D2366-14	16.2	517	718	0.7	0.1245	0.0051	0.0181	0.0002	115	1.3
D2366-15	5.2	162	223	0.7	0.1298	0.0082	0.0180	0.0003	115	1.8
D2366-17	11.7	364	534	0.7	0.1146	0.0054	0.0179	0.0002	114	1.4
D2366-18	2.5	65	117	0.6	0.1272	0.0087	0.0177	0.0004	113	2.3
D2366-19	16.7	406	797	0.5	0.1241	0.0049	0.0178	0.0003	114	1.7
D2366-21	5.8	196	264	0.7	0.1129	0.0061	0.0177	0.0003	113	1.8
D2366-22	6.0	201	267	0.8	0.1250	0.0079	0.0178	0.0003	114	1.9
D2366-25	9.6	299	441	0.7	0.1153	0.0060	0.0176	0.0002	113	1.5
D2366-26	9.8	277	463	0.6	0.1284	0.0066	0.0176	0.0003	112	1.6
D2366-28	8.4	450	319	1.4	0.1219	0.0064	0.0178	0.0002	114	1.6
D2366-30	11.2	317	522	0.6	0.1230	0.0055	0.0176	0.0002	112	1.5

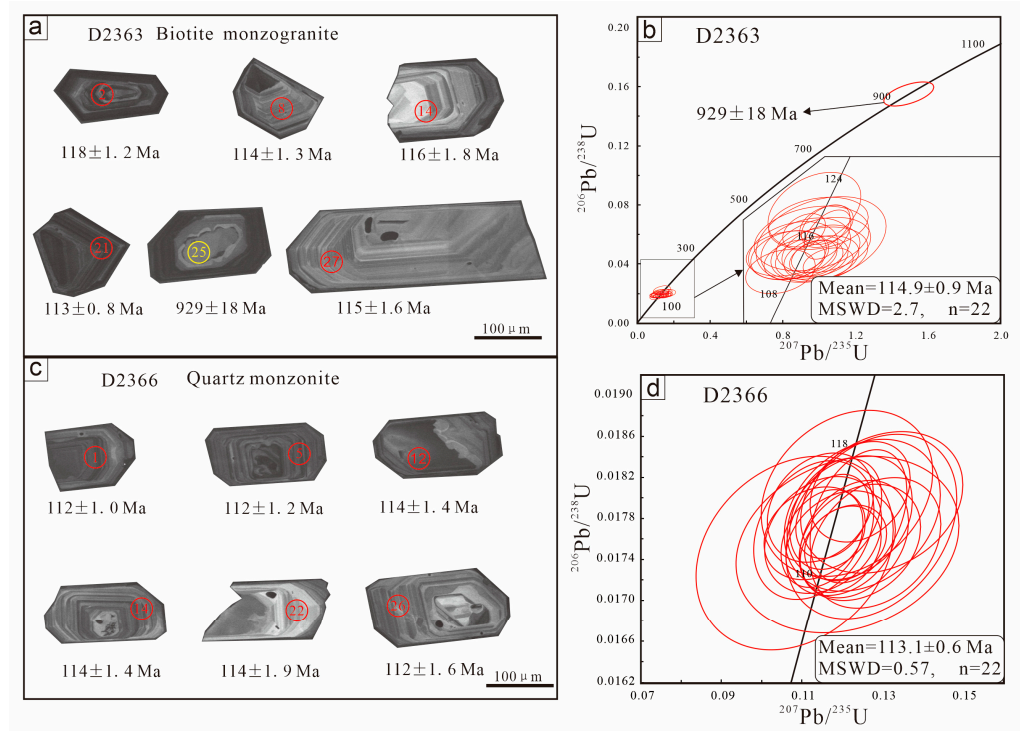


Figure 3. Cathodoluminescence (CL) images of representative zircon grains from biotite monzogranite ((a), sample D2363) and quartz monzonite ((c), sample D2366). Concordia plots of zircon from biotite monzogranite ((b), sample D2363) and quartz monzonite ((d), sample D2366). The corresponding weighted average $^{207}\text{Pb}/^{206}\text{Pb}$ age diagrams of zircons with high concordance (>95) are used for plots. Magmatic zircons are marked in red. Inherited zircon domain is marked in the yellow circle.

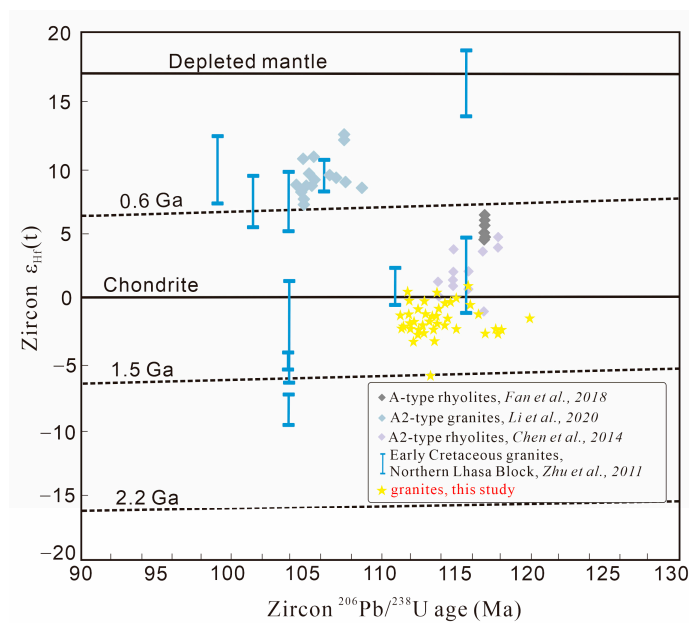


Figure 4. Zircon $^{206}\text{Pb}/^{238}\text{U}$ vs. Zircon $\epsilon_{\text{Hf}}(t)$ and diagrams of the Burshulaling Granites and A (or A2)-type granites, rhyolites, and Early Cretaceous granites along the BNSZ [21,28,29,31].

Table 2. LA-ICP-MS zircon Hf isotopic data of the Burshulaling Granites.

Point	Ages (Ma)	$^{176}\text{Yb}/^{177}\text{Hf}$	1 σ	$^{176}\text{Hf}/^{177}\text{Hf}$	1 σ	$^{176}\text{Lu}/^{177}\text{Hf}$	1 σ	$\epsilon_{\text{Hf}}(0)$	$\epsilon_{\text{Hf}}(t)$	T_{DM} (Ma)	T_{DM}^{C} (Ma)	$f_{\text{Lu/Hf}}$
D2363-02	118	0.054295	0.002399	0.282628	0.000013	0.001721	0.000089	-5.1	-2.6	900	1339	-0.95
D2363-05	114	0.031156	0.000223	0.282669	0.000014	0.001003	0.000013	-3.7	-1.2	826	1247	-0.97
D2363-06	115	0.030894	0.000336	0.282635	0.000014	0.000965	0.000009	-4.8	-2.4	873	1322	-0.97
D2363-07	120	0.042053	0.000644	0.282649	0.000014	0.001332	0.000025	-4.3	-1.8	861	1289	-0.96
D2363-08	114	0.021805	0.000176	0.282645	0.000013	0.000695	0.000004	-4.5	-2.1	853	1300	-0.98
D2363-09	118	0.074151	0.000446	0.282618	0.000014	0.002355	0.000013	-5.4	-3	930	1364	-0.93
D2363-11	117	0.142634	0.004410	0.282666	0.000016	0.004224	0.000139	-3.8	-1.5	908	1267	-0.87
D2363-12	113	0.032751	0.000446	0.282656	0.000013	0.000978	0.000007	-4.1	-1.7	844	1277	-0.97
D2363-13	117	0.074383	0.000179	0.28262	0.000015	0.002285	0.000004	-5.4	-3	926	1361	-0.93
D2363-14	116	0.030295	0.000452	0.282679	0.000014	0.000946	0.000016	-3.3	-0.8	810	1222	-0.97
D2363-15	118	0.027974	0.000274	0.282624	0.000012	0.000274	0.000015	-5.2	-2.7	887	1344	-0.97
D2363-16	115	0.023157	0.000307	0.282683	0.000014	0.000753	0.000009	-3.1	-0.7	800	1213	-0.98
D2363-17	116	0.019409	0.000077	0.282719	0.000012	0.000638	0.000002	-1.9	0.6	747	1130	-0.98
D2363-19	115	0.025402	0.000372	0.282686	0.000013	0.000372	0.000001	-3.0	-0.6	798	1206	-0.97
D2363-20	114	0.034504	0.001628	0.282706	0.000015	0.001101	0.000048	-2.3	0.1	775	1163	-0.97
D2363-21	113	0.050703	0.000466	0.282622	0.000011	0.001596	0.000013	-5.3	-2.9	906	1355	-0.95
D2363-23	112	0.030186	0.000099	0.282629	0.000014	0.000988	0.000004	-5.0	-2.7	881	1337	-0.97
D2363-24	114	0.084543	0.001134	0.28265	0.000016	0.002557	0.000025	-4.3	-2	889	1296	-0.92
D2363-26	114	0.006518	0.000067	0.282527	0.000012	0.000205	0.000003	-8.7	-6.2	1005	1562	-0.99
D2366-01	112	0.052516	0.002292	0.282638	0.000013	0.001724	0.000079	-6.0	-2.4	887	1396	-0.97
D2366-02	114	0.048036	0.000440	0.282603	0.000013	0.001559	0.000015	-2.8	-3.6	932	1194	-0.98
D2366-04	112	0.095200	0.001723	0.282695	0.000018	0.002916	0.000045	-4.8	-0.5	831	1323	-0.97
D2366-05	112	0.032529	0.000143	0.282603	0.000011	0.001018	0.000002	-4.9	-3.6	919	1327	-0.95
D2366-06	115	0.022135	0.000141	0.282692	0.000011	0.000687	0.000004	-3.9	-0.4	787	1266	-0.97
D2366-07	112	0.031263	0.000801	0.282635	0.000012	0.000964	0.000024	-3.8	-2.4	872	1260	-0.96
D2366-09	113	0.051599	0.000991	0.282635	0.000012	0.00159	0.000041	-4.8	-2.5	888	1320	-0.97
D2366-10	112	0.033289	0.000407	0.282661	0.000015	0.001048	0.000012	-2.2	-1.5	838	1156	-0.97
D2366-11	112	0.037606	0.000103	0.282664	0.000012	0.001181	0.000006	-5.1	-1.4	837	1338	-0.98
D2366-12	114	0.032850	0.001036	0.282636	0.000013	0.001016	0.000028	-4.3	-2.4	872	1285	-0.98
D2366-13	112	0.032916	0.001992	0.28271	0.000013	0.001038	0.000065	-4.3	0.2	768	1285	-0.97
D2366-14	115	0.026127	0.000310	0.282628	0.000012	0.000812	0.000004	-2.9	-2.6	880	1201	-0.97
D2366-15	115	0.021164	0.000087	0.282651	0.000013	0.000701	0.000003	-4.2	-1.8	844	1280	-0.97
D2366-17	114	0.028872	0.000122	0.282652	0.000013	0.000961	0.000004	-5.0	-1.8	849	1334	-0.98
D2366-18	113	0.034857	0.000852	0.28269	0.000013	0.001104	0.000003	-2.9	-0.5	799	1197	-0.98
D2366-19	114	0.025911	0.000147	0.282654	0.000013	0.000834	0.000002	-3.6	-1.8	844	1243	-0.98
D2366-21	113	0.023946	0.000129	0.28263	0.000012	0.000724	0.000004	-5.2	-2.6	874	1348	-0.98
D2366-22	114	0.023801	0.000090	0.28269	0.000013	0.00073	0.000004	-6.9	-0.4	790	1316	-0.97
D2366-25	113	0.023172	0.000209	0.28267	0.000013	0.00075	0.000003	-8.5	-1.2	818	1330	-0.97
D2366-26	112	0.025076	0.000142	0.282624	0.000011	0.00082	0.000002	-10.2	-2.8	885	1343	-0.97

$\epsilon_{\text{Hf}}(t) = \{ [((^{176}\text{Hf}/^{177}\text{Hf})_{\text{Sample}} - (^{176}\text{Lu}/^{177}\text{Hf})_{\text{Sample}} \times (e^{\lambda t} - 1)) / ((^{176}\text{Hf}/^{177}\text{Hf})_{\text{CHUR}} - (^{176}\text{Lu}/^{177}\text{Hf})_{\text{CHUR}} \times (e^{\lambda t} - 1))] - 1 \} \times 100,000$; $T_{\text{DM}} = 1/\lambda \times \ln \{ 1 + [((^{176}\text{Hf}/^{177}\text{Hf})_{\text{Sample}} - (^{176}\text{Hf}/^{177}\text{Hf})_{\text{DM}}) / ((^{176}\text{Lu}/^{177}\text{Hf})_{\text{Sample}} - (^{176}\text{Lu}/^{177}\text{Hf})_{\text{DM}})] \}$; $T_{\text{DM}}^{\text{C}} = T_{\text{DM}} - (T_{\text{DM}} - t) \times [(f_{\text{CC}} - f_{\text{S}}) / (f_{\text{CC}} - f_{\text{DM}})]$; f_{CC} , f_{S} and f_{DM} represent the $f_{\text{Lu/Hf}}$ values of continental crust, zircon samples and depleted mantle, respectively. $f_{\text{CC}} = -0.55$, $f_{\text{DM}} = 0.16$, $f_{\text{S}} = (^{176}\text{Hf}/^{177}\text{Hf})_{\text{Sample}} / (^{176}\text{Lu}/^{177}\text{Hf})_{\text{CHUR}} - 1$; $(^{176}\text{Hf}/^{177}\text{Hf})_{\text{CHUR}} = 0.282772$, $(^{176}\text{Lu}/^{177}\text{Hf})_{\text{CHUR}} = 0.0332$, $(^{176}\text{Hf}/^{177}\text{Hf})_{\text{DM}} = 0.28325$, $(^{176}\text{Lu}/^{177}\text{Hf})_{\text{DM}} = 0.0384$. $\lambda = 1.867 \times 10^{-11} \text{ a}^{-1}$, $t = ^{206}\text{Pb}/^{238}\text{U}$ age.

4.3. Whole-Rock Major- and Trace-Element Results

The geochemical results of the analysis of 7 granite samples from the Burshulaling are given in Table 3. These granites are high in SiO_2 (72.6–76.4 wt.%), K_2O (4.1–5.9 wt.%), Na_2O (2.8–3.6 wt.%), and low in Al_2O_3 (12.2–13.5 wt.%), CaO (0.5–1.4 wt.%). All samples show a high content of total alkalis (ALK, as calculated in Table 3, the same as below) of 7.6–8.7 wt.% and a low CaO content of 0.5–1.4 wt.% (Table 3). The aluminum saturation index A/CNK is between 1.03 and 1.12, A/NK ratio is between 1.19 and 1.32, showing peraluminous characteristics (Figure 5a; Table 3). In the SiO_2 - K_2O diagram, the Burshulaling Granites plot into the high-K calc-alkaline area (Figure 5b). Seven samples have high Ga content (18.3–24.3 ppm) and Ga/Al ratio (2.61–3.47), and low Sr (24.5–60.4 ppm), Ba (99.4–179 ppm), Ti (683–1890 ppm) and P (213–550 ppm) content. Low Zr (103–209 ppm) and Nb (16–31 ppm) contents and high Zr/Hf (20.9–30.0) and Nb/Ta (4.5–11.2) ratios are characteristic of all granite samples (Table 3). In the chondrite-normalized REE diagrams (Figure 6a), the granite samples show enrichment in LREE [(La/Yb)_N = 3.11–8.58], with strong negative Eu anomalies [$2 \times \text{Eu}/(\text{Sm} + \text{Gd})$, 0.08–0.20]. In the primitive mantle-normalized diagrams (Figure 6b), the Burshulaling Granites show depletion of Sr [$2 \times \text{Sr}/(\text{Ce} + \text{Nd})$, 0.03–0.08], Ba [$2 \times \text{Ba}/(\text{Rb} + \text{Th})$, 0.02–0.05] and Ti [$2 \times \text{Ti}/(\text{Sm} + \text{Tb})$, 0.03–0.06]. Zircon saturation temperatures were determined according to the model of Watson and Harrison (1983) [55], which was established mainly based on experiments at 860–1020 °C, but also proved to be valid at $M(\text{Na} + \text{K} + 2\text{Ca}/(\text{Al}-\text{Si})) = 1.3$, corresponding to temperatures up to 1500 °C. The calculated results are between 1028 and 1085 °C with an average of 1049 °C.

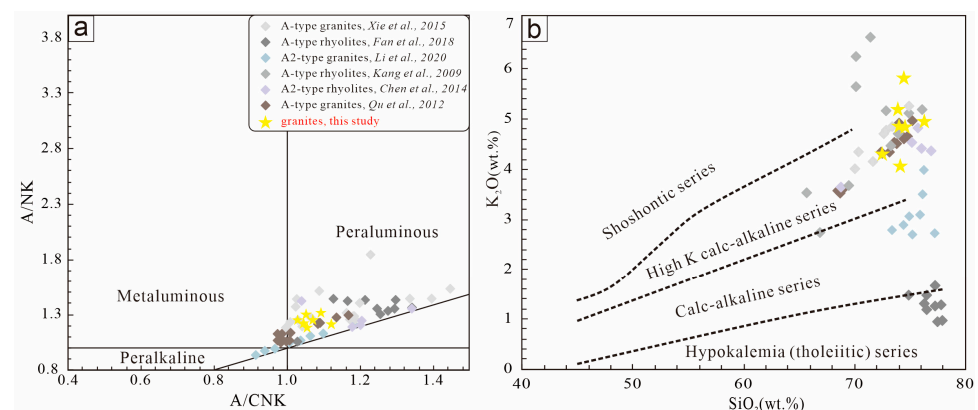


Figure 5. A/CNK vs. A/NK (a) and SiO_2 vs. K_2O (b) and diagrams of the Burshulaling Granites and A (or A2)-type granites, rhyolites along the northern margin of the Lhasa Block [28–32].

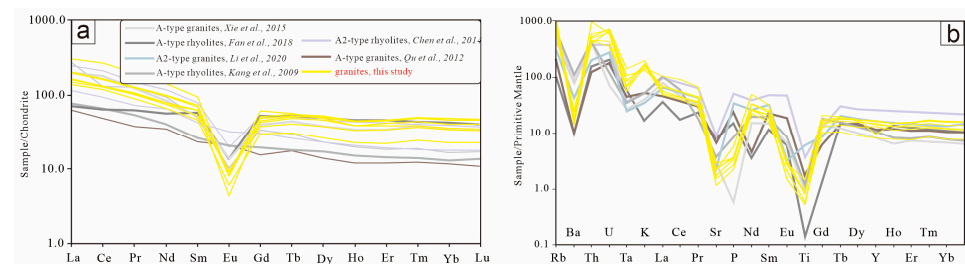


Figure 6. Chondrite-normalized REE distribution patterns (a) and primitive mantle-normalized spidergrams (b) of the Burshulaling Granites and A (or A2)-type granites, rhyolites along the northern margin of the Lhasa Block [28–32].

Table 3. Major (wt.%), trace, and earth element (ppm) analysis results of the Burshulaling Granites.

Sample	D2360	D2361	D2362	D2363	D2364	D2365	D2366
SiO ₂	74.50	73.97	74.65	74.18	72.60	76.44	74.12
Al ₂ O ₃	13.24	13.46	13.09	13.11	13.22	12.24	13.19
FeO	0.33	1.19	1.13	1.45	1.95	0.94	0.69
Fe ₂ O ₃	0.75	0.36	0.50	0.18	0.96	0.29	0.96
Na ₂ O	2.80	3.19	3.26	3.58	3.24	2.92	3.19
K ₂ O	5.89	5.26	4.85	4.11	4.35	5.03	4.92
MgO	0.15	0.24	0.23	0.30	0.43	0.16	0.31
CaO	0.48	1.11	1.09	1.07	1.37	0.74	1.19
MnO	0.03	0.04	0.04	0.04	0.06	0.03	0.04
P ₂ O ₅	0.05	0.08	0.07	0.08	0.13	0.06	0.08
TiO ₂	0.11	0.18	0.18	0.19	0.32	0.13	0.18
LOI	0.93	0.57	1.01	1.07	0.46	0.39	0.61
Total	99.27	99.66	100.11	99.36	99.09	99.37	99.46
Zr	116.7	133.7	131.3	144.2	208.8	102.8	126.0
Hf	5.59	4.46	5.04	5.77	7.33	3.71	4.99
La	35.60	38.60	46.50	47.70	72.50	33.10	39.10
Ce	77.70	81.00	97.50	101.00	164.00	72.50	80.60
Pr	9.62	9.87	11.80	12.30	18.70	8.58	10.20
Nd	35.10	35.50	45.30	46.20	66.90	30.60	37.10
Sm	9.57	8.12	10.70	11.30	14.50	7.16	9.49
Eu	0.25	0.53	0.46	0.46	0.47	0.35	0.54
Gd	9.33	7.78	10.00	10.50	12.50	6.19	8.86
Tb	1.94	1.53	1.99	2.08	2.14	1.15	1.81
Dy	13.00	9.48	12.80	13.40	12.40	6.73	11.80
Ho	2.50	1.86	2.46	2.57	2.20	1.27	2.20
Er	7.57	5.69	7.47	7.69	6.41	3.68	6.85
Tm	1.28	0.93	1.24	1.29	0.98	0.63	1.11
Yb	8.20	5.87	7.82	7.96	6.06	3.81	6.91
Lu	1.20	0.85	1.19	1.19	0.89	0.57	1.03
Be	8.16	6.12	6.11	10.30	7.10	6.07	6.58
V	4.70	8.09	7.53	9.72	14.90	5.23	9.67
Cr	10.70	17.50	14.30	10.00	13.70	8.68	11.40
Ni	0.71	1.93	1.34	1.98	2.33	1.44	2.85
Ga	18.30	21.10	21.90	21.90	24.30	19.60	21.20
Rb	772	510	538	420	492	530	550
Sr	24.5	49	36.4	47.4	46.1	32.2	60.4
Nb	26.3	20.2	22.6	24.2	31.2	16.3	21.3
Cd	0.038	0.031	0.028	0.098	0.039	0.036	0.029
Cs	21	12.6	19.5	28.4	40.5	13.4	20.1
Ba	114	171	134	130	128	99.4	179
Ta	5.88	2.9	3.6	4.42	2.78	2.33	3.52
Ti	3.65	2.19	2.47	2.4	2.33	2.26	2.44
Pb	49.1	51.4	54.7	49.2	47.5	52.3	55.5
Th	43.7	37.7	50.4	33.2	91	38.8	42.2
U	15.2	7.47	14.4	14.1	12.5	9.18	13.2
Y	78	59.8	74.1	43.8	66.1	36.9	68
Zr/Hf	20.9	30.0	26.1	25.0	28.5	27.7	25.3
Nb/Ta	4.5	6.9	6.3	5.5	11.2	7.0	6.1
M	1.37	1.33	1.26	1.38	1.36	1.37	1.31
T (°C)	1042.4	1045.3	1044.9	1055.5	1085.0	1028.6	1040.6
Ga/Al	2.61	2.96	3.16	3.15	3.47	3.02	3.04
δEu	0.08	0.20	0.14	0.13	0.11	0.16	0.18
δCe	1.03	1.02	1.02	1.02	1.09	1.05	0.99
A/CNK	1.12	1.04	1.04	1.07	1.05	1.06	1.04
A/NK	1.21	1.23	1.23	1.27	1.32	1.19	1.25
La/Yb	4.34	6.58	5.95	5.99	11.96	8.69	5.66
Sr/Y	0.31	0.82	0.49	1.08	0.70	0.87	0.89

LOI = loss on ignition; $\delta_{Eu} = [2 \times Eu / (Sm + Gd)]_N$; $\delta_{Ce} = [2 \times Ce / (La + Pr)]_N$; A/CNK = Al/(Ca + Na + K) (molar ratio); A/NK = Al/(Na + K) (molar ratio); M = (Na + K + 2Ca)/(Al-Si) (molar ratio); T(zr) = $12,900 / [2.95 + 0.85 \times M + \ln(496,000 / Zr_{melt})]$.

5. Discussion

5.1. Explanation of Zircon U-Pb Ages

The analyses of zircons from samples D2363 and D2366 (22 zircons for each) yield ²⁰⁶Pb/²³⁸U ages 115 Ma and 113 Ma, respectively. All zircon grains in both granite samples (D2363 and D2366) have clear oscillational zoning structures and high Th/U ratios, suggest-

ing a magmatic origin. This indicates that the Burshulaling Granites formed and intruded into the Northern Lhasa Block at ca. 115–113 Ma. The inherited zircon from sample D2363 yields a $^{206}\text{Pb}/^{238}\text{U}$ age of 929 ± 18 Ma, representing the age of crustal components in the parent magma. Similar ages (ca. 1000–800 Ma) have a strong record on the Tibetan Plateau, most of which are associated with the Rodinia supercontinent [56]. For example, Xu et al. (2010) and Guo et al. (2017) obtained ca. 1000 Ma zircon age from the gneiss of the Nangagbarwa Group in the eastern Himalayan [56,57]. Hu et al. (2016) obtained 925 Ma zircon age from the Northern Lhasa Block metamorphic gabbro [58]. The Ando and Basu areas produced a high abundance of detrital zircon grains with ages intervals of 920–820 Ma [59–61]. These zircon grains from ancient crust are preserved in the juvenile granite during the partial melting.

5.2. Assessment of Element Mobility of the Burshulaling Granites

Previous studies have shown that alkali elements such as K and Na, and LILE such as Rb, Sr, and Ba are mobile during post-magmatic alteration, while the HFSE such as Th, Nb, Ta, Zr, Hf, and Ti, and REE behave oppositely [62,63]. The Lhasa Block experienced metamorphism and deformation in the India–Asia collision with a record of massive magmatic activity [12,64]. The petrography of the Burshulaling Granites shows a slight alteration characteristic (Figure 2a). Some plagioclase grains exhibit features of sericitization and clayization, while biotite grains are characterized by chloritization and carbonatization (Figure 2d–f). Therefore, it is essential to evaluate the influence of post-magmatic change on the chemical constituents of the Burshulaling Granites. Lower LOI values (0.39–1.07) and narrow Ce/Ce* ratios [$2 \times \text{Ce}/(\text{La} + \text{Pr})$, 0.99–1.09] indicate that no chemical components of the sampled rocks were mobilized post-magmatically. The concentrated distribution of the granites in the zircon $^{206}\text{Pb}/^{238}\text{U}$ against $\varepsilon_{\text{Hf}}(t)$ also demonstrates that they are not significantly altered (Figure 4). Meanwhile, this characteristic is consistent with the chondrite- and primitive mantle-normalized diagram. No metamorphic rims from zircon grains can be observed (Figure 3a,c). The geometrical characteristics and zircon structures reveal that the host rocks did not undergo a significant alteration by late metamorphism and deformation. The weak alteration suggests that it can utilize mobile elements such as Na, K, Ca, Al, Rb, and Ga and immobile elements such as V, Ti, Zr, Y, Ce, and Nb to decipher the petrogenesis and tectonic environment.

5.3. Petrogenesis of the Burshulaling Granites

5.3.1. An A2-Type Affinity of the Burshulaling Granites

Loiselle and Wones (1979) introduced the concept of A-type granites (alkaline, anhydrous, and anorogenic) as distinct from the I-, M-, and S-type granites. “A” represents alkaline, anhydrous, and anorogenic, indicating that most A-type granites were generated in a non-orogenic environment [1]. However, new statistics show that most juvenile A-type granites are orogen-related (>75%), and only rift-hotspot-related A-type granites should be interpreted as characteristic of within-plate or intra-cratonic settings [65]. Geochemically, A-type granites are marked by high SiO_2 , FeO^{T} , $\text{Na}_2\text{O} + \text{K}_2\text{O}$, REE concentrations, and Ga/Al ratios, but low Al_2O_3 , Sr, Ba, Eu (<0.30), Ti concentrations (Figure 7a–c) [2–6]. The Burshulaling Granites are marked by high SiO_2 , K_2O , Ga, total alkalis, low Al_2O_3 , and CaO concentrations and show peraluminous characteristics (Figure 5a), high-K calc-alkaline series (Figure 5b, Table 3). In the normalized diagrams, the Burshulaling Granites show features of strongly negative Eu, Sr, Ba, and Ti anomalies (Figure 6a,b). These characteristics agree with typical A-type granites [2,6,7]. In the $10,000\text{Ga}/\text{Al}$ against $(\text{K}_2\text{O} + \text{Na}_2\text{O})$, Y, and Nb diagram, all of them fall within the A-type granites area (Figure 7a–c) [7]. Furthermore, it is noted that the Burshulaling Granites have a similar geochemical composition to typical A-type granites from the Northern Lhasa Block of the same age (Figure 7a–c). Eby (1992) further classified A-type granites into A1 and A2. A1-type granites show similar element ratio characteristics to oceanic-island basalt, formed in a within-plate environment [10]. A2-type granites show similar element ratio characteristics from continental crust to island-

arc basalts formed in a post-collision environment [10]. All Burshulaling Granites samples fall within the A2 granites area in the diagram of Y/Nb against Rb/Nb, Nb-Y-3Ga, and Nb-Y-Ce (Figure 8a–c) [10]. Thus, we can conclude that the Early Cretaceous Burshulaling Granites belong to the A2-type granites.

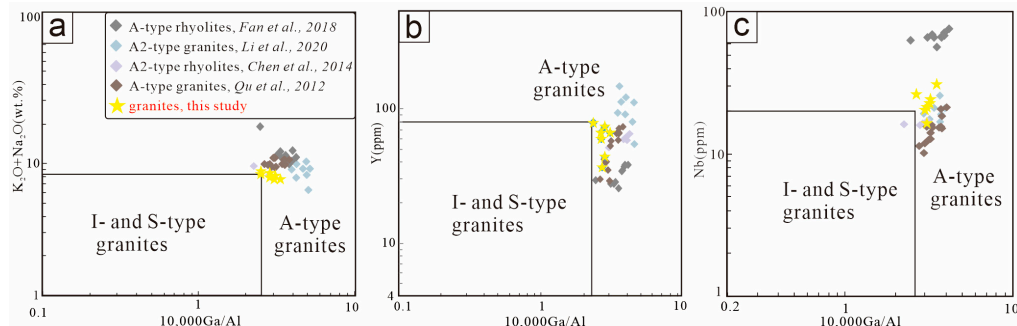


Figure 7. ($K_2O + Na_2O$) vs. $10,000Ga/Al$ (a), Y vs. $10,000Ga/Al$ (b), and Nb vs. $10,000Ga/Al$ (c) diagrams of the Burshulaling Granites and A(or A2)-type granites, rhyolites along the northern margin of the Lhasa Block [7,28,29,31,32].

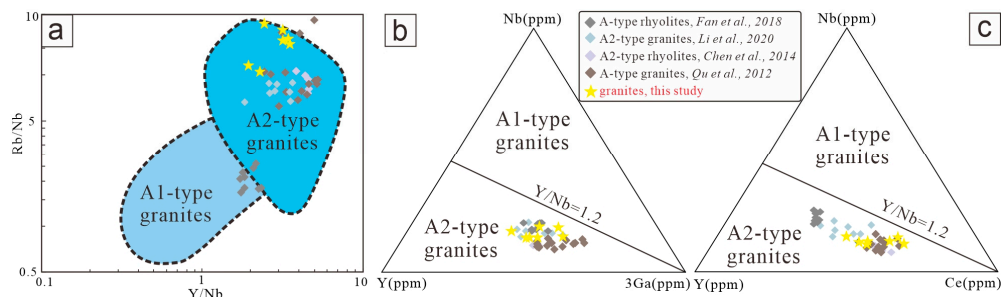


Figure 8. Rb/Nb vs. Y/Nb (a), Nb vs. Y vs. 3Ga (b), and Nb vs. Y vs. Ce (c) diagrams of the Burshulaling Granites and A(or A2)-type granites, rhyolites along the northern margin of the Lhasa Block [10,28,29,31,32].

5.3.2. Magma Source of the A-Type Granite

Previous research about the generation of A-type granites is disputed. It mainly includes two opinions: (i) partial melting of the ancient continental crust [66], and (ii) fractional crystallization involves the mafic magma that originates from the Earth's mantle, which process can occur with or without the addition of felsic magma from the crust [4,67,68]. The high siliceous and potassic contents but low magnesium and chromium contents (Table 3) indicate that the Burshulaling Granites were probably associated with partially melting continental crusts. In addition, an inherited zircon domain in biotite monzonite (D2363) with an age of ca. 929 Ma suggests that these rocks were predominantly formed through the melting of continental crusts. Meanwhile, the $\epsilon_{Hf}(t)$ value (D2363, varied from -6.2 to $+0.6$; D2366, varied from -3.6 to $+0.2$) shows obvious characteristics of crust-mantle interaction (Figure 4). Therefore, these felsic rocks may have been produced by the melting of continental crust but are partially influenced by mantle material.

Zircon saturation temperatures are calculated between 1028 and 1085 °C with an average of 1049 °C by the model after Watson and Harrison (1983) [55], which is interpreted as the lowest temperature of magma melting because the zircon crystallized during the cooling process. The zircon saturation temperatures agree with typical A-type granites [8], while they are greater than typical I- or S-type granites. In the $Al_2O_3 + MgO + TiO_2 + Fe_2O_3^T$ against $Al_2O_3/(MgO + TiO_2 + Fe_2O_3^T)$ diagram, all samples from the Burshulaling Granites plot into the area near the line of low pressure (Figure 9a) [69]. Different residual phases usually indicate different melting pressures. Grt with little or no Pl means that plagioclase is always retained during the melting process, which generally occurs in a low pressure

environment [70]. In the La/Yb against Sr/Y diagram, samples from the Burshulaling Granites are plotted into the stability field of Grt with little or no PI (Figure 9b) [71]. All granites have significant negative Eu anomalies (0.08–0.20), indicating strong enrichment of plagioclase in the residual phases of the magma. Overall, our findings reveal that parental magma of the Burshulaling Granites was generated in a low pressure environment. From our results, we note that the Burshulaling Granites were formed under low pressure (Figure 9a) and high temperatures (1028–1085 °C, Table 3) conditions, consistent with experimental studies of the formation conditions for A-type granites [2,66]. These features constrain that Burshulaling A-type granites might be formed in a tectonic setting of crustal thinning (low pressure) and asthenosphere mantle upwelling (high temperatures) [2]. The models for crustal thinning include orogenic root detachment, lithospheric root convective thinning, and slab break-off [72]. The upwelling of the asthenosphere mantle caused by slab break-off can provide high heat flow for partial melting. The upwelling asthenosphere material, enriched oceanic slabs, and upper continental crust provide a variety of materials for the magma source (Figure 10a). All these characteristics indicate that the A-type Burshulaling granitic magma might be generated under a low pressure–high temperature environment caused by slab break-off. However, the possibility of gravity-induced orogenic root detachment cannot be ruled out in consideration of the thickening of the Late Mesozoic Lhasa Block. The Jurassic–Lower Cretaceous sediments thickened by more than 10 km during this period, resulting in the covering of a quarter of the Lhasa Block [15]. The confluence of a thickened upper crust and the Early Cretaceous Lassa Block within an extensional context resulted in the detachment of orogenic roots (Figure 10b). The A-type Burshulaling granites have a high SiO₂ (72.6–76.4 wt.%) content and low Zr/Hf (20.9–30.0) and Nb/Ta (4.5–11.2) ratios (Table 3), indicating that they belong to moderately to highly fractionated granites [73,74].

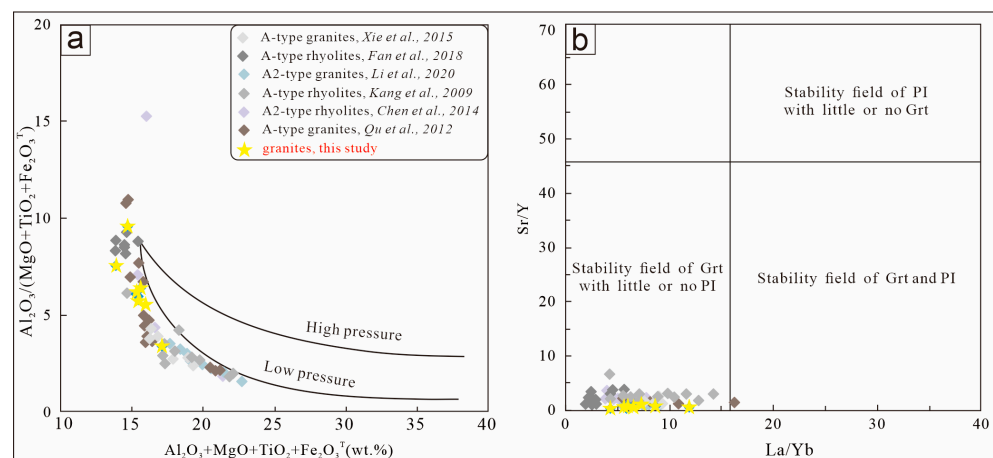


Figure 9. $\text{Al}_2\text{O}_3 + \text{MgO} + \text{TiO}_2 + \text{Fe}_2\text{O}_3^{\text{T}}$ vs. $\text{Al}_2\text{O}_3/(\text{MgO} + \text{TiO}_2 + \text{Fe}_2\text{O}_3^{\text{T}})$ (a) and Sr/Y vs. La/Yb (b) diagrams of the Burshulaling Granites and A(or A2)-type granites, rhyolites along the northern margin of the Lhasa Block [27–32,69,71]. Abbreviations: Grt = garnet, PI = plagioclase.

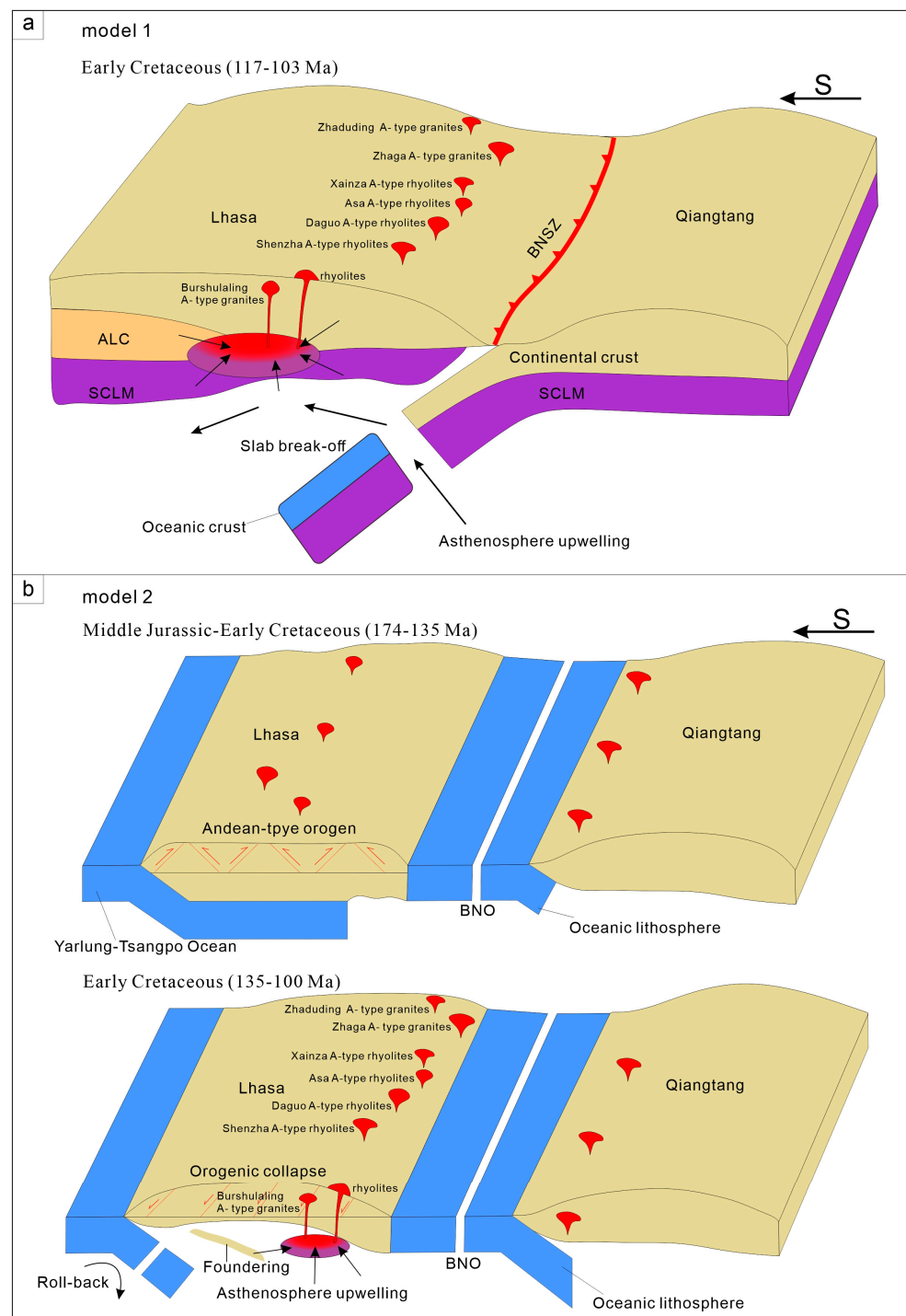


Figure 10. Two possible schematic models show the origin of the Early Cretaceous A-type acidic magmatic belt in the Northern Lhasa Block (a) During the Early Cretaceous (117–103 Ma), the slab break-off occurred after southward subduction of the BNO and resulting in A-type acidic magmatism within the North Lhasa Block [15]. (b) During the Jurassic–Early Cretaceous (174–135 Ma), the flat subduction of the Yarlung–Zangpo oceanic crust resulted in the formation of an Andean-type orogen within the Lhasa Block. Subsequently (135–100 Ma), the delamination of the lithosphere and asthenosphere upwelling resulted in forming A-type acidic magmatism [21]. Abbreviations: BNSZ: Bangong–Nujiang suture zone, BNO: Bangong–Nujiang Ocean, ALC: ancient lower crust, SCLM: sub-continental lithospheric mantle.

5.4. The A-Type Acidic Magmatic Belt in the Northern Lhasa Block

The Early Cretaceous granites are mainly distributed in Central and Northern Lhasa Blocks [13,14,21,50] but may have been eroded by Tibetan Plateau uplift and erosion in Southern Lhasa Block [75]. Zircons within the Central Lhasa Block demonstrate the feature of negative zircon $\varepsilon_{\text{Hf}}(t)$, while those within the Northern Lhasa Block show transitional characteristics. The zircon $\varepsilon_{\text{Hf}}(t)$ demonstrates a monotonic increase from the eastern Northern Lhasa Block to the western Northern Lhasa Block. From a negative anomaly dominance (−10 to +0.9 eastern) to a positive anomaly slightly negative (−1.5 to +10.1 center) and further to a strong positive negative (+4.7 to +18.4 western) [21] (Figure 4). Our results of the zircon $\varepsilon_{\text{Hf}}(t)$ (−6.2 to +0.6 in the eastern segment of Northern Lhasa Block, Table 2) are in good agreement with these characteristics (Figure 4). Both central and northern granites have variable Silicic contents, high-K calc-alkaline series, and metaluminous–peralkaline [21]. Most felsic magmatism shows the features of either I- or S-type, and it is widely acknowledged that these granites were formed as a result of the subduction of oceanic lithosphere, occurring in a syn-collisional setting [21], which differs from the Burshulaling Granites in a post-collisional setting. The A-type (or A2-type) acidic magmatism is reported only in a limited area in the Northern Lhasa Block and presents high SiO_2 contents and weak peraluminous–metaluminous series (Figure 5a,b). Xie et al. (2015) reported 103 Ma Zhaduding A-type granites generated in a post-collisional setting due to the upwelling of asthenosphere material from the western segment of the Northern Lhasa Block [27]. At the same time, many researchers mentioned A-type (or A2-type) acidic magmatism from the Northern Lhasa Block middle segment, which is generated by the partial melting during BNO crust subduction (e.g., 117–112 Ma, Fan et al., 2018; 107–105 Ma, Li et al., 2020; 117–112 Ma, Kang et al., 2009; 117–115 Ma, Chen et al., 2014; 114–110 Ma, Qu et al., 2012) [28–32]. Although the origin of these granites is hotly debated, they are all typical A-type granites in their chemical composition. The above-counted A-type or A2-type acidic magmatism are all located near the northern boundary of the Lhasa Block and formed during the same age (117–103 Ma). The differences in their $\varepsilon_{\text{Hf}}(t)$ may related to the different contributions of mantle-crust components in the magma source. The similar $\varepsilon_{\text{Hf}}(t)$ compositions of the A-type granites indicate that they formed during the same conditions and period of subduction (Figure 4). However, the existence of A-type granites has never been identified from the eastern segment of the Northern Lhasa Block. Combining with the published data from related granites/rhyolites (Figure 8a–c), we propose the existence of an Early Cretaceous magmatic belt with A-type characteristics within the North Lhasa Block, which formed in a similar post-collisional environment.

5.5. Implications for Southward Subduction of BNO or Orogenic Collapse of Lhasa Block

The BNSZ is over 1200 km long, stretching from west to east, and marks the boundary separating Qiangtang and Lhasa Blocks, and is mainly composed of Jurassic–Cretaceous flysch, (ophiolite) mélangé, and volcanic rocks [11,12]. The formation process of BNSZ is accompanied by the subduction of BNO, but the polarity of subduction remains controversial. Two perspectives on BNO subduction polarity have been proposed: only a single northward subduction or divergent double subduction. Researchers suggested southward subduction mainly based on the arc-related rocks in the Northern Lhasa Block [13,14,21]. For example, 134–125 Ma Andesite–dacite–rhyolite granitoids with low-K to high-K calc-alkaline series, positive zircon $\varepsilon_{\text{Hf}}(t)$ are abundantly exposed in the Baingoin area [21]. Here, we propose one possible explanation that the Early Cretaceous A-type (A2-type) post-collisional acidic magmatic belt is related to the BNO southward subduction. In addition to the arc-related granite responses to the southward subduction event within the Lhasa Block, there is typical post-collision A-type acidic magmatism. Angular unconformity contacts at different areas within the BNSZ show that the Lhasa–Qiangtang collision was earlier in the east than in the west, and the final close time should be earlier than ~113 Ma [11,21,76,77]. Therefore, the Qiangtang–Lhasa collision in the Burshulaling area should be earlier than 113 Ma. The easternmost segment of the Lhasa Block has transitioned to a post-collision

environment at ca. 115–113 Ma, which is confirmed by our geochronological and geochemical data. Recently, a dense broadband magnetotelluric profile transecting the BNZS revealed a zone of inclined electrical gradient, both northward and southward [78]. The electrical gradient zone was interpreted as the subduction BNO [78]. Both geophysical and geochemical evidence further support the existence of bidirectional subduction. The A-type (or A2-type) acidic magmatic belt along the BNSZ in many areas is the response to the collision of the Qiangtang-Lhasa Block (Figure 10a). This over 1200 km long belt and the ubiquitous syn-collisional granites within the Lhasa Block document the complete process of BNO closure and continent-continent collision.

Nevertheless, evidence from Late Jurassic–Middle Cretaceous ophiolite fragments and marine sediments indicates that the BNO did not close before the Late Cretaceous [15,16,20]. Concurrently, there is evidence that the magmatic arcs in the southern Qiangtang Block (161–100 Ma) result from the northward subduction of the BNO [20,34]. Paleomagnetic evidence also suggests that the BNSZ was still a broad ocean during the Cretaceous [79]. Consequently, it is unlikely that the A-type acidic magmatism of a post-collisional setting could have formed. A more plausible explanation for forming A-type acidic magmatism is the hypothesis of orogenic collapse. The available evidence lends support to this hypothesis. During the Jurassic–Early Cretaceous (174–135 Ma), the flat subduction of the Yarlung–Zangpo oceanic crust resulted in the formation of an Andean-type orogen within the Lhasa Block. This process was accompanied by crustal thickening, syn-orogenic magmatism, and thrusting [15]. Subsequently, the entire Lhasa Block was transformed from a compressional deformation to an extensional deformation [15]. The delamination of the lithosphere and asthenosphere upwelling together provided the requisite material and heat for the formation of the A-type acidic magmatism (Figure 10b). The observed differences in their $\epsilon_{\text{Hf}}(t)$ values may be attributed to the degree of lithospheric exchange involved in the process of foundering. It was not until the Late Cretaceous that the BNO was closed by subduction to the north [15,16,20].

The orogenic collapse appears to be a more plausible explanation, yet considerable evidence also supports the southward subduction of the BNO. While the onset and termination of this southward subduction remain uncertain, it cannot be entirely ruled out that those A-type granites originated from this process. Accordingly, the possibility remains open that the A-type granites were formed by southward subduction of the BNO or a collapse following an Andean-type orogeny.

6. Conclusions

The study reaches the following conclusions:

- (1) Geochemical data show that the Burshulaling Granites are peraluminous high-K calc-alkaline, A-type granites formed in a high temperature–low pressure post-collision environment and underwent a moderately to highly fractionated process.
- (2) The 115–113 Ma Burshulaling Granites were formed by the mixing of upwelling of the asthenosphere and the melting of the lower crust due to slab break-off or orogenic root detachment.
- (3) There is an A-type acidic magmatic belt along the northern margin of the Lhasa Block, which indicates that the BNO subducted to the south or that an Andean-type orogen collapsed.

Author Contributions: Conceptualization, D.X. and X.Y.; methodology, D.X.; formal analysis, D.X. and X.Y.; investigation, D.X., C.T., T.C., N.Z. and J.C.; data curation, D.X.; writing—original draft preparation, D.X.; writing—review and editing, D.X. and T.C.; visualization, D.X.; supervision, X.Y.; project administration, X.Y.; funding acquisition, D.X. and X.Y. All authors have read and agreed to the published version of the manuscript.

Funding: This research was funded by Geological Investigation Project from China Geological Survey, grant numbers DD20221814 and DD20230138, and Innovation Fund (No. CXJJ2024-04) from the Cores and Samples Center of Natural Resources, China Geological Survey, Langfang, China.

Data Availability Statement: Data are contained within the article.

Acknowledgments: We are grateful to the editors and three reviewers for their constructive reviews and comments that substantially improved this work.

Conflicts of Interest: The authors declare no conflict of interest.

References

1. Loisel, M.C.; Wones, D.R. Characteristics and origin of anorogenic granites. *GSA Bull.* **1979**, *11*, 468.
2. Zhang, Q.; Ran, H.; Li, C.D. A-type granite: What is the essence? *Acta Petrol. Mineral.* **2012**, *31*, 621–626. [[CrossRef](#)]
3. Bonin, B. A-type granites and related rocks: Evolution of a concept, problems and prospects. *Lithos* **2007**, *97*, 1–29. [[CrossRef](#)]
4. Frost, C.D.; Frost, B.R. On ferroan (A-type) granitoids: Their compositional variability and modes of origin. *J. Petrol.* **2011**, *52*, 39–53. [[CrossRef](#)]
5. Dall’Agnol, R.; de Oliveira, D.C. Oxidized, magnetite-series rapakivi-type granites of Carajás, Brazil: Implications for classification and petrogenesis of A-type granites. *Lithos* **2007**, *93*, 215–233. [[CrossRef](#)]
6. Collins, W.J.; Huang, H.Q.; Bowden, P.; Kemp, A.I.S. Repeated S–I–A-type granite trilogy in the Lachlan Orogen, and geochemical contrasts with A-type granites in Nigeria: Implications for petrogenesis and tectonic discrimination. *Geol. Soc. London* **2020**, *491*, 53–76. [[CrossRef](#)]
7. Whalen, J.; Currie, K.; Chappell, B. A-type granites: Geochemical characteristics, discrimination and petrogenesis. *Contrib. Miner. Petrol.* **1987**, *95*, 407–419. [[CrossRef](#)]
8. King, P.L.; Chappell, B.W.; Allen, C.M.; White, A.J.R. Are A-type granites the high temperature felsic granites? Evidence from fractionated granites of the Wangrah Suite. *Aust. J. Earth Sci.* **2001**, *48*, 501–514. [[CrossRef](#)]
9. Eby, G.N. The A-type granitoids: A review of their occurrence and chemical characteristics and speculations on their petrogenesis. *Lithos* **1990**, *26*, 115–134. [[CrossRef](#)]
10. Eby, G.N. Chemical subdivision of the A-type granitoids: Petrogenetic and tectonic implications. *Geology* **1992**, *20*, 641–644. [[CrossRef](#)]
11. Yin, A.; Harrison, T.M. Geological evolution of the Himalayan-Tibetan Orogen. *Annu. Rev. Earth Planet. Sci.* **2000**, *28*, 211–280. [[CrossRef](#)]
12. Pan, G.T.; Wang, L.Q.; Li, R.S.; Yuan, S.H.; Ji, W.H.; Yin, F.G.; Zhang, W.P.; Wang, B.D. Tectonic evolution of the Qinghai-Tibet Plateau. *J. Asian Earth Sci.* **2012**, *53*, 3–14. [[CrossRef](#)]
13. Zhu, D.C.; Zhao, Z.D.; Niu, Y.L.; Dilek, Y.; Hou, Z.Q.; Mo, X.X. The origin and pre-Cenozoic evolution of the Tibetan Plateau. *Gondwana Res.* **2013**, *23*, 1429–1454. [[CrossRef](#)]
14. Zhu, D.C.; Li, S.M.; Cawood, P.A.; Wang, Q.; Zhao, Z.D.; Liu, S.A.; Wang, L.O. Assembly of the Lhasa and Qiangtang terranes in central Tibet by divergent double subduction. *Lithos* **2016**, *245*, 7–17. [[CrossRef](#)]
15. Zhang, K.J.; Zhang, Y.X.; Tang, X.C.; Xia, B. Late Mesozoic tectonic evolution and growth of the Tibetan plateau prior to the Indo-Asian collision. *Earth-Sci. Rev.* **2012**, *114*, 236–249. [[CrossRef](#)]
16. Zhang, K.J.; Xia, B.; Zhang, Y.X.; Liu, W.L.; Zeng, L.; Li, J.F.; Xu, L.F. Central Tibetan Meso-Tethyan oceanic plateau. *Lithos* **2014**, *210*, 278–288. [[CrossRef](#)]
17. Song, Y.; Tang, J.X.; Lin, B.; Yang, C.; Sun, H. Metallogeny in the Bangong–Nujiang belt, central Tibet, China: A review. *Front. Earth Sci.* **2023**, *11*, 2296–6463. [[CrossRef](#)]
18. Kapp, P.; Murphy, M.A.; Yin, A.; Harrison, T.M.; Ding, L.; Guo, J.H. Mesozoic and Cenozoic tectonic evolution of the Shiquanhe area of western Tibet. *Tectonics* **2003**, *22*, 1029. [[CrossRef](#)]
19. Kapp, P.; Yin, A.; Harrison, T.M.; Ding, L. Cretaceous-Tertiary shortening, basin development, and volcanism in central Tibet. *GSA Bull.* **2005**, *117*, 865–878. [[CrossRef](#)]
20. Chen, W.Y.; Hu, X.C.; Zhong, Y.; Fu, Y.B.; Li, F.; Wang, Y.G. Comment on “Sedimentary and tectonic evolution of the southern Qiangtang basin: Implications for the Lhasa-Qiangtang collision timing” by A. Ma et al. *J. Geophys. Res. Solid Earth* **2018**, *123*, 7338–7342. [[CrossRef](#)]
21. Zhu, D.C.; Zhao, Z.D.; Niu, Y.L.; Mo, X.X.; Chung, S.L.; Hou, Z.Q.; Wang, L.O.; Wu, F.Y. The Lhasa Terrane: Record of a microcontinent and its histories of drift and growth. *Earth Planet. Sci. Lett.* **2011**, *301*, 241–255. [[CrossRef](#)]
22. Van Lente, B.; Ashwal, L.; Pandit, M.; Bowring, S.; Torsvik, T. Neoproterozoic hydrothermally altered basaltic rocks from Rajasthan, northwest India: Implications for late Precambrian tectonic evolution of the Aravalli Craton. *Precambrian Res.* **2009**, *170*, 202–222. [[CrossRef](#)]
23. Coulon, C.; Megartsi, M.; Fourcade, S.; Maury, R.; Bellon, H.; Louni-Hacini, A.; Cotton, J.; Coutelle, A.; Hermitte, D. Post-collisional transition from calc-alkaline to alkaline volcanism during the Neogene in Oranie (Algeria): Magmatic expression of a slab breakoff. *Lithos* **2002**, *62*, 87–110. [[CrossRef](#)]
24. Van Hunen, J.; Allen, M.B. Continental collision and slab break-off: A comparison of 3-D numerical models with observations. *Earth Planet. Sci. Lett.* **2011**, *302*, 27–37. [[CrossRef](#)]
25. Zeng, Y.C.; Chen, J.L.; Xu, J.F.; Wang, B.D.; Huang, F. Sediment melting during subduction initiation: Geochronological and geochemical evidence from the Darutso high-Mg andesites within ophiolite mélange, central Tibet. *Geochem. Geophys. Geosyst.* **2016**, *17*, 4859–4877. [[CrossRef](#)]

26. Peng, Y.B.; Yu, S.Y.; Li, S.Z.; Liu, Y.J.; Dai, L.M.; Lv, P.; Guo, R.H.; Liu, Y.M.; Wang, Y.H.; Xie, W.M. Early Jurassic and Late Cretaceous granites in the Tongka micro-block, Central Tibet: Implications for the evolution of the Bangong-Nujiang ocean. *J. Asian Earth Sci.* **2020**, *194*, 1367–9120. [[CrossRef](#)]
27. Xie, L.; Dun, D.; Zhu, L.D.; Nima, C.; Yang, W.G.; Tao, G.; Li, C.; He, B.; He, Y. Zircon U-Pb geochronology, geochemistry and geological significance of the Zhaduding A-type granites in northern Gangdese, Tibet. *Geol. China* **2015**, *42*, 1214–1227. [[CrossRef](#)]
28. Fan, J.J.; Li, C.; Sun, Z.M.; Xu, W.; Wang, M.; Xie, C.M. Early cretaceous MORB-type basalt and A-type rhyolite in northern Tibet: Evidence for ridge subduction in the Bangong-Nujiang Tethyan Ocean. *J. Asian Earth Sci.* **2018**, *154*, 187–201. [[CrossRef](#)]
29. Li, H.; Wang, M.; Zeng, X.W.; Luo, A.B.; Yu, Y.P.; Zeng, X.J. Slab break-off origin of 105 Ma A-type porphyritic granites in the Asa area of Tibet. *Geol. Mag.* **2020**, *157*, 1281–1298. [[CrossRef](#)]
30. Kang, Z.Q.; Xu, J.F.; Wang, B.D.; Dong, Y.H.; Wang, S.Q.; Chen, J.L. Geochemistry of Cretaceous volcanic rocks of Duoni formation in Northern Lhasa Block: Discussion of Tectonic setting. *Earth Sci. China Univ. Geosci.* **2009**, *34*, 89–104. [[CrossRef](#)]
31. Chen, Y.; Zhu, D.C.; Zhao, Z.D.; Meng, F.Y.; Wang, Q.; Santosh, M.; Wang, L.Q.; Dong, G.C.; Mo, X.X. Slab breakoff triggered ca. 113 Ma magmatism around Xainza area of the Lhasa Terrane, Tibet. *Gondwana Res.* **2014**, *26*, 449–463. [[CrossRef](#)]
32. Qu, X.M.; Wang, R.J.; Xin, H.B.; Jiang, J.H.; Chen, H. Age and petrogenesis of A-type granites in the middle segment of the Bangonghu-Nujiang suture, Tibetan plateau. *Lithos* **2012**, *146*, 264–275. [[CrossRef](#)]
33. Zhang, K.J.; Zhang, Y.X.; Tang, X.C.; Xie, Y.W.; Sha, S.L.; Peng, X.J. First report of eclogites from central Tibet, China: Evidence for ultradeep continental subduction prior to the Cenozoic India-Asian collision. *Terra Nova* **2008**, *20*, 302–308. [[CrossRef](#)]
34. Hu, X.M.; Ma, A.L.; Xue, W.W.; Garzanti, E.; Cao, Y.; Li, S.M.; Sun, G.Y.; Lai, W. Exploring a lost ocean in the Tibetan Plateau: Birth, growth, and demise of the Bangong-Nujiang Ocean. *Earth-Sci. Rev.* **2022**, *229*, 104031. [[CrossRef](#)]
35. Liu, W.B.; Qian, Q.; Yue, G.L.; Li, Q.S.; Zhang, Q.; Zhou, M.F. The geochemical characteristics of fore-arc ophiolite from Dingqing area, Tibet. *Acta Petrol. Sin.* **2020**, *18*, 392–400. [[CrossRef](#)]
36. Guynn, J.H.; Kapp, P.; Pullen, A.; Heizler, M.; Gehrels, G.; Ding, L. Tibetan basement rocks near Amdo reveal “missing Mesozoic tectonism along the Bangong suture, central Tibet. *Geology* **2006**, *34*, 505–508. [[CrossRef](#)]
37. Tang, Y.; Zhai, O.G.; Hu, P.Y.; Xiao, X.C.; Wang, H.T.; Wang, W.; Zhu, Z.C.; Wu, H. Jurassic high-Mg andesitic rocks in the middle part of the Bangong-Nujiang suture zone. Tibet: New constraints for the tectonic evolution of the Meso-Tethys Ocean. *Acta Petrol. Sin.* **2019**, *35*, 3097–3114. [[CrossRef](#)]
38. Wang, X.C.; Xia, B.; Liu, W.L.; Zhong, Y.; Hu, X.C.; Guan, Y.; Huang, W.; Yin, Z.X. Geochronology, geochemistry and petrogenesis of the Pungco ophiolite, Tibet. *Geotecton. Metallog.* **2018**, *42*, 550–569. [[CrossRef](#)]
39. Zeng, M.; Zhang, X.; Cao, H.; Ettensohn, F.R.; Chen, W.; Lang, X. Late Triassic initial subduction of the Bangong-Nujiang Ocean beneath Oiangtang revealed: Stratigraphic and geochronological evidence from Gaize, Tibet. *Basin Res.* **2014**, *28*, 147–157. [[CrossRef](#)]
40. Li, S.; Ding, L.; Guilmette, C.; Fu, J.; Xu, O.; Yue, Y.; Henrique-Pinto, R. The subduction-accretion history of the Bangong-Nujiang Ocean: Constraints from provenance and geochronology of the Mesozoic strata near Gaize, central Tibet. *Tectonophysics* **2017**, *702*, 42–60. [[CrossRef](#)]
41. Ji, C.; Yan, L.L.; Lu, L.; Jin, X.; Huang, Q.T.; Zhang, K.J. Anduo Late Cretaceous high-K calc-alkaline and shoshonitic volcanic rocks in central Tibet, western China: Relamination of the subducted Meso-Tethyan oceanic plateau. *Lithos* **2021**, *400*, 106345. [[CrossRef](#)]
42. Zhang, W.Q.; Liu, C.Z.; Liu, T.; Zhang, C.; Zhang, Z.Y. Subduction initiation triggered by accretion of a Jurassic oceanic plateau along the Bangong–Nujiang Suture in central Tibet. *Terra Nova* **2021**, *33*, 150–158. [[CrossRef](#)]
43. Baxter, A.T.; Aitchison, J.C.; Zyabrev, S.V. Radiolarian age constraints on Meso-Tethyan ocean evolution, and their implications for development of the Bangong-Nujiang suture, Tibet. *J. Geol. Soc.* **2009**, *166*, 689–694. [[CrossRef](#)]
44. Shi, R.D.; Griffin, W.L.; O’Reilly, S.Y.; Huang, Q.T.; Zhang, X.R.; Liu, D.L. Melt/mantle mixing produces podiform chromite deposits in ophiolites: Implications of Re-Os systematics in the Dongqiao Neo-tethyan ophiolite, northern Tibet. *Gondwana Res.* **2012**, *21*, 194–206. [[CrossRef](#)]
45. Chen, L.; Zhao, Z.F. Origin of continental arc andesites: The composition of source rocks is the key. *J. Asian Earth Sci.* **2017**, *145*, 217–232. [[CrossRef](#)]
46. Fan, S.Y.; Ding, L.; Murphy, M.A.; Yao, W.; Yin, A. Late Paleozoic and Mesozoic evolution of the Lhasa Terrane in the Xainza area of southern Tibet. *Tectonophysics* **2017**, *721*, 415–434. [[CrossRef](#)]
47. Huang, T.T.; Xu, J.F.; Chen, J.L.; Wu, J.B.; Zeng, Y.C. Sedimentary record of Jurassic northward subduction of the Bangong-Nujiang Ocean: Insights from detrital zircons. *Int. Geol. Rev.* **2017**, *59*, 166–184. [[CrossRef](#)]
48. Li, Q.H.; Lu, L.; Zhang, K.J.; Yan, L.L.; Huangfu, P.; Hui, J.; Ji, C. Late Cretaceous post-orogenic delamination in the western Gangdese arc: Evidence from geochronology, petrology, geochemistry, and Sr–Nd–Hf isotopes of intermediate–acidic igneous rocks. *Lithos* **2022**, *424*, 106763. [[CrossRef](#)]
49. Zhang, Y.X.; Li, Z.W.; Yang, W.G.; Zhu, L.D.; Jin, S.; Zhou, X.Y.; Tao, G.; Zhang, K.J. Late Jurassic–Early Cretaceous episodic development of the Bangong Meso-Tethyan subduction: Evidence from elemental and Sr–Nd isotopic geochemistry of arc magmatic rocks, Gaize region, central Tibet, China. *J. Asian Earth Sci.* **2017**, *135*, 212–242. [[CrossRef](#)]
50. Pan, G.T.; Ding, J.; Yao, D.S.; Wang, L.Q. *Guidebook of 1:1,500,000 Geologic Map of the Qinghai–Xizang (Tibet) Plateau and Adjacent Areas*; Cartographic Publishing House: Chengdu, China, 2004; pp. 1–148.

51. Ding, L.; Kapp, P.; Wan, X. Paleocene–Eocene record of ophiolite obduction and initial India–Asia collision, south-central Tibet. *Tectonics* **2005**, *24*, TC3001. [[CrossRef](#)]
52. Liu, Y.S.; Gao, S.; Hu, Z.C.; Gao, C.G.; Zong, K.Q.; Wang, D.B. Continental and oceanic crust recycling-induced melt-peridotite interactions in the Trans-North China Orogen: U–Pb dating, Hf isotopes and trace elements in zircons of mantle xenoliths. *J. Petrol.* **2010**, *51*, 537–571. [[CrossRef](#)]
53. Hu, Z.C.; Zhang, W.; Liu, Y.S.; Gao, S.; Li, M.; Zong, K.Q.; Chen, H.H.; Hu, S.H. “Wave” signal-smoothing and mercury-removing device for laser ablation quadrupole and multiple collector ICPMS analysis: Application to lead isotope analysis. *Anal. Chem.* **2015**, *87*, 1152–1157. [[CrossRef](#)] [[PubMed](#)]
54. Hoskin, P.W.; Schaltegger, U. The composition of zircon and igneous and metamorphic petrogenesis. *Rev. Mineral. Geochem.* **2003**, *53*, 27–62. [[CrossRef](#)]
55. Watson, E.B.; Harrison, T.M. Zircon saturation revisited: Temperature and composition effects in a variety of crustal magma types. *Earth Planet. Sci. Lett.* **1983**, *64*, 295–304. [[CrossRef](#)]
56. Xu, W.C.; Zhang, H.F.; Parrish, R.; Harris, N.; Guo, L.; Yuan, H.L. Timing of granulite-facies metamorphism in the eastern himalayan syntaxis and its tectonic implications. *Tectonophysics* **2010**, *485*, 231–244. [[CrossRef](#)]
57. Guo, L.; Wang, C.; Zhang, H.F.; Harris, N.; Pan, F.B. Detrital zircon u-pb geochronology, trace-element and hf isotope geochemistry of the metasedimentary rocks in the eastern himalayan syntaxis: Tectonic and paleogeographic implications. *Gondwana Res.* **2017**, *41*, 207–221. [[CrossRef](#)]
58. Hu, P.; Zhai, Q.; Tang, Y.; Wang, H.; Wu, H. The middle Neoproterozoic meta-gabbro from the north Lhasa terrane of Tibet and its geological implications. *Geol. Bull. China* **2016**, *37*, 1400–1405.
59. Guynn, J.H.; Kapp, P.; Gehrels, G.E.; Ding, L. U–Pb geochronology of basement rocks in central Tibet and paleogeographic implications. *J. Asian Earth Sci.* **2012**, *43*, 23–50. [[CrossRef](#)]
60. Zhang, Z.M.; Dong, X.; Liu, F.; Lin, Y.H.; Yan, R.; Santosh, M. Tectonic Evolution of the Amdo Terrane, Central Tibet: Petrochemistry and Zircon U–Pb Geochronology. *J. Geology* **2012**, *120*, 431–451. [[CrossRef](#)]
61. Liu, Y.; Wang, Y.; Li, S.; Santosh, M.; Yu, S. Neoproterozoic amdo and jiayuqiao microblocks in the tibetan plateau: Implications for rodinia reconstruction. *GSA Bull.* **2020**, *133*, 663–678. [[CrossRef](#)]
62. Polat, A.; Hofmann, A.W. Alteration and geochemical patterns in the 3.7–3.8 Ga Isua greenstone belt, West Greenland. *Precambrian Res.* **2003**, *126*, 197–218. [[CrossRef](#)]
63. Ordóñez-Calderón, J.C.; Polat, A.; Fryer, B.J.; Gagnon, J.E.; Raith, J.G.; Appel, P.W.U. Evidence for HFSE and REE mobility during calc-silicate metasomatism, Mesoproterozoic (~3075 Ma) Ivisartaq greenstone belt, southern West Greenland. *Precambrian Res.* **2008**, *161*, 317–340. [[CrossRef](#)]
64. Pearce, J.A.; Deng, W. The ophiolites of the Tibet geotraverse, Lhasa to Golmud (1985) and Lhasa to Kathmandu (1986). *Philos. Trans. R. Soc. A* **1988**, *327*, 215–238. [[CrossRef](#)]
65. Condie, K.C.; Pisarevsky, S.A.; Puetz, S.J.; Roberts, N.M.W.; Spencer, C.J. A-type granites in space and time: Relationship to the supercontinent cycle and mantle events. *Earth Planet. Sci. Lett.* **2023**, *610*, 118125. [[CrossRef](#)]
66. Patiño Douce, A.E.P. Generation of metaluminous A-type granites by low pressure melting of calc-alkaline granitoids. *Geology* **1997**, *25*, 743–746. [[CrossRef](#)]
67. Yang, J.H.; Wu, F.Y.; Chung, S.L.; Wilde, S.A.; Chu, M.F. A hybrid origin for the Qianshan A-type granite, northeast China: Geochemical and Sr\Nd\Hf isotopic evidence. *Lithos* **2006**, *89*, 89–106. [[CrossRef](#)]
68. Shellnutt, J.G.; Wang, C.Y.; Zhou, M.F.; Yang, Y.H. Zircon Lu–Hf isotopic compositions of metaluminous and peralkaline A-type granitic plutons of the Emeishan large igneous province (SW China): Constraints on the mantle source. *J. Asian Earth Sci.* **2009**, *35*, 45–55. [[CrossRef](#)]
69. Douce, P. Amphibolite to granulite transition in aluminous greywackes from the Sierra de Comechingones, Córdoba, Argentina. *J. Metamorph. Geol.* **1999**, *17*, 415–434. [[CrossRef](#)]
70. Martin, H.; Smithies, R.H.; Rapp, R.; Moyen, J.F.; Champion, D. An overview of adakite, tonalite-trondhjemite-granodiorite (TTG), and sanukitoid: Relationships and some implications for crustal evolution. *Lithos* **2005**, *79*, 1–24. [[CrossRef](#)]
71. Rapp, R.P.; Watson, E.B. Dehydration melting of metabasalt at 8–32 kbar: Implications for continental growth and crust-mantle recycling. *J. Petrol.* **1995**, *36*, 891–931. [[CrossRef](#)]
72. Wang, W.; Pandit, M.K.; Zhao, J.H.; Chen, W.T.; Zheng, J.P. Slab break-off triggered lithosphere-asthenosphere interaction at a convergent margin: The Neoproterozoic bimodal magmatism in NW India. *Lithos* **2018**, *296*, 281–296. [[CrossRef](#)]
73. Wu, F.Y.; Liu, X.C.; Ji, W.Q.; Wang, J.M.; Yang, L. Highly fractionated granites: Recognition and research. *Sci. China Earth Sci.* **2017**, *60*, 1201–1219. [[CrossRef](#)]
74. Ballouard, C.; Poujol, M.; Boulvais, P.; Branquet, Y.; Tartèse, R.; Vigneresse, J.L. Nb-Ta fractionation in peraluminous granites: A marker of the magmatic-hydrothermal transition. *Geology* **2016**, *44*, 231–234. [[CrossRef](#)]
75. Wu, F.Y.; Ji, W.Q.; Liu, C.Z.; Chung, S.L. Detrital zircon U–Pb and Hf isotopic data from the Xigaze fore-arc basin: Constraints on Transhimalayan magmatic evolution in southern Tibet. *Chem. Geol.* **2010**, *271*, 13–25. [[CrossRef](#)]
76. Zhang, K.J.; Xia, B.D.; Wang, G.M.; Li, Y.T.; Ye, H.F. Early Cretaceous stratigraphy, depositional environments, sandstone provenance, and tectonic setting of central Tibet, western China. *GSA Bull.* **2004**, *116*, 1202–1222. [[CrossRef](#)]
77. Kapp, P.; DeCelles, P.G.; Gehrels, G.E.; Heizler, M.; Ding, L. Geological records of the Lhasa Qiangtang and Indo-Asian collisions in the Nima area of central Tibet. *GSA Bull.* **2007**, *119*, 917–933. [[CrossRef](#)]

78. Liang, H.D.; Fang, H.; Xiao, D.; Zhong, Q.; He, M.X.; Pei, F.G.; Wang, G.; Zhang, X.B.; Bai, D.W.; Lü, Q.Y. Divergent double subduction of Bangong-Nujiang Ocean revealed by high-resolution magnetotelluric data at 86° E in the northern Tibetan Plateau. *Tectonophysics* **2023**, *862*, 229960. [[CrossRef](#)]
79. Otofuji, Y.I.; Mu, C.L.; Tanaka, K.; Miura, D.; Inokuchi, H.; Kamei, R.; Tamai Takemoto, K.; Zaman, H.; Yokoyama, M. Spatial gap between Lhasa and Qiangtang blocks inferred from Middle Jurassic to Cretaceous paleomagnetic data. *Earth Planet. Sci. Lett.* **2007**, *262*, 581–593. [[CrossRef](#)]

Disclaimer/Publisher’s Note: The statements, opinions and data contained in all publications are solely those of the individual author(s) and contributor(s) and not of MDPI and/or the editor(s). MDPI and/or the editor(s) disclaim responsibility for any injury to people or property resulting from any ideas, methods, instructions or products referred to in the content.